This paper is part of the Proceedings of the 11th International Conference
on Engineering Sciences (AFM 2016)
www.witconferences.com

Numerical simulations of the aerodynamic response of 2D circular segments by means of URANS

F. Nieto, M. Cid Montoya, A. Álvarez, S. Hernández
& J. Á. Jurado
Structural Mechanics group, School of Civil Engineering,
Universidade da Coruña, Spain

Abstract

In the wind engineering field, the so-called D-section (semi-circular cylinder) has attracted some attention from researchers, since it is a galloping prone geometry. In fact, a modest number of references where this type of cross-section has been studied in the wind tunnel can be found, such as Novak and Tanaka (1974) or Weaver and Veljkovic (2005). However, to the authors' knowledge, references in the literature concerning the CFD-based simulation of the aerodynamic response of circular segments are particularly scarce. In this work a 2D Unsteady Reynolds-Averaged Navier–Stokes (URANS) approach has been adopted with the purpose of computing force coefficients and Strouhal numbers of static circular segments at the subcritical regime considering corner angles of $90°$, $80°$, $70°$, $60°$, $50°$ and $40°$. Since the motivation of this work is to study circular segments as a simplified bridge deck geometry, the reference flow direction is parallel to the rectilinear side. It has been found that this kind of cross-section is particularly challenging since it presents massive flow separation on the rectilinear side, as well as the inherent difficulties in modeling the aerodynamic response on curved surfaces at high Reynolds numbers. For certain geometrical configurations low-Reynolds-number and curvature corrections in the $k - \omega$ Shear-Stress Transport (SST) turbulence model had to be introduced, as well as considering transition from laminar to turbulent flow, in order to obtain results similar to the experimental data.

Keywords: URANS, turbulence models, semicircular cylinder, wind tunnel.

1 Introduction

This works aims to characterize the aerodynamic behavior of circular segment cylinders subject to shape variations in their height, as shown in figure 1, which is defined by the value of the β parameter in the range $[40°, 90°]$. This study is of interest in the frame of carrying out a shape optimization of a simplified bridge deck cross-section [1].

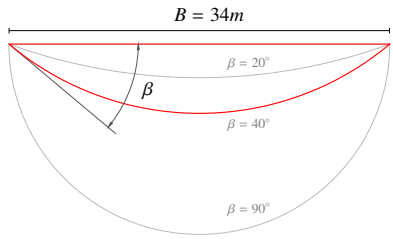

Figure 1: Deck cross-section employed with the angle β as the only shape parameter.

Figure 2: View of the Art Institute footbridge in Chicago, USA.

The $\beta = 90°$ section, also known as D-section, was firstly studied by Den Hartog [2] and later by Richardson and Martuccelli [3] in order to study the galloping effects on conductors. The effects of turbulence over the $\beta = 90°$ section are dealt with in [4], while [5] also studies the vortex shedding phenomena over this section. In the CFD realm, lift and drag coefficients were obtained in [6] for the D-section, in the frame of energy harvesting studies based on flow-induced vibrations.

New shapes in bridge decks design are nowadays considered in bridges and footbridges. This includes the presence of circular-based shapes and cross-section shapes very similar to slender circular segments. This is the case, for instance, of the Santander footbridge [7] in Spain, a balcony beam of 70.7 meters long with curved layout and a steel-concrete composite semicircular section. Another footbridge with the same cross-section can be found in Chicago, USA, known as the Art Institute footbridge, which is shown in figure 2. Another circular shape is employed in the Riyadh metro cross-section, which correspond to approximately $\beta = 50°$. Besides, some slender cross-section of newly build long-span bridges are very similar to these sections for low values of β. This is the case for instance of the Yavuz Sultan Selim Bridge, in Istanbul, Turkey.

The presence of curved shapes in the cross-section of this kind of structures is due to its aesthetic quality, as is the case of the Den Haag station viaducts, in the Netherlands. The use of these new shapes in the cross sections of common

structures increase the interest in curved cross section as the ones studied in this work.

2 Formulation

2.1 Force coefficients

The target of this study is to obtain the aerodynamic coefficients and Strouhal numbers of the circular segments for the sections $\beta = [40°, 50°, 60°, 70°, 80°, 90°]$. These aerodynamic properties are defined as

$$C_L = \frac{L}{\frac{1}{2}\rho U^2 B}, \quad C_D = \frac{D}{\frac{1}{2}\rho U^2 B}, \quad C_M = \frac{M}{\frac{1}{2}\rho U^2 B^2} \quad \text{and} \quad St = \frac{fH}{U}, \tag{1}$$

where L, D and M are the time-averaged lift, drag and moment forces per unit of length, with the sign indicated in figure 3, U is the wind velocity, ρ is the flow density, B and H are the width and height of the section and f the vortex shedding frequency.

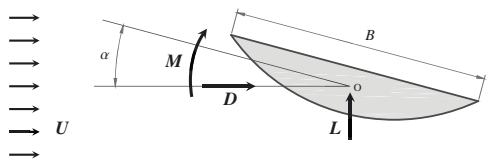

Figure 3: Sign convection adopted for the aerodynamic coefficients.

2.2 Governing equations

The numerical computation of the aerodynamic forces is carried out for the sections studied in this work by means of a 2-D Unsteady Reynolds-Averaged Navier-Stokes (URANS) approach. This methodology is widely described in [8–10] among several others, and a brief summary is outlined below.

The effects of the wind around the deck sections is modeled by the unsteady Reynolds-averaged Navier-Stokes equations considering incompressible flow, which means that

$$\frac{\partial \rho}{\partial t} = 0, \tag{2}$$

where ρ is the density of the fluid, which is assumed constant in the whole domain, and t represents the time. The Reynolds averaged equations of motion

in conservative form according to [11] are expressed in tensor notation for the three space dimensions as

$$\frac{\partial U_i}{\partial x_i} = 0, \tag{3}$$

$$\rho \frac{\partial U_i}{\partial t} + \rho U_j \frac{\partial U_i}{\partial x_j} = -\frac{\partial P}{\partial x_i} + \frac{\partial}{\partial x_j}\left(2\mu S_{ij} - \rho\overline{u_i{}' u_j{}'}\right), \tag{4}$$

where U_i is the averaged flow velocity vector, x_i the position vector, P is the mean pressure, μ is the viscosity of the fluid, S_{ij} is the strain-rate tensor, which is defined as

$$S_{ij} = \frac{1}{2}\left[\frac{\partial u_i}{\partial x_j} + \frac{\partial u_j}{\partial x_i}\right], \tag{5}$$

and $u_i{}'$ is the fluctuation velocity and $\overline{u_i{}'}$ its time average. The term $-\overline{u_i{}' u_j{}'}$ in eq. (4) defines the specific Reynolds stress tensor

$$\tau_{ij} = -\overline{u_i{}' u_j{}'}, \tag{6}$$

which can be modeled based on the Boussinesq assumption [11]

$$\tau_{ij} = 2\nu_T S_{ij} - \frac{2}{3} k \delta_{ij}. \tag{7}$$

where ν_T is the kinematic eddy viscosity and k is the turbulent kinetic energy per unit of mass.

2.3 Turbulence models

The solution of the closure problem is carried out through turbulence models. The turbulence models based on the Boussinesq assumption (eq. (7)) are known as the viscosity models, and perhaps the most popular are the Spalart–Allmara model [12], the standard $k-\epsilon$ model [11], the RGN $k-\epsilon$ model [13], the Wilcox $k-\omega$ model [14] and the Menter's Shear-Stress Transport (SST) $k-\omega$ model [15, 16]. A brief and useful summary of them can be found in [17].

In order to characterize the aerodynamic behavior of the sections considered in this study, several turbulence models, corrections and implementations have been adopted, employing the open source code OpenFOAM [18] and the ANSYS Fluent [19] software. The problem is firstly tackled using the two-equation Menter's $k-\omega$ SST model for incompressible flows, as described in [20]. Later, some corrections are applied in order to improve the characterization of the aerodynamic responses of the cross-sections studied. Finally, the four-equation transition SST model is also considered. A summary of these is presented next.

2.3.1 Menter's $k-\omega$ SST model

The SST $k-\omega$ model aims to take advantage of the robust and accurate formulation of the $k-\omega$ model in the near-wall region and the $k-\epsilon$ model performance in the far field, avoiding the sensitivity of the results to the freestream values specified for

k and ω characteristics of the $k-\omega$ model. It was first developed by Menter in [15] and improved in [20], and it is similar to the $k-\omega$ model although it includes some refinements. Further information may be found in [19], and the formulation is presented below

$$\frac{\partial}{\partial t}(\rho k)+\frac{\partial}{\partial x_i}(\rho k u_i)=\frac{\partial}{\partial x_j}\left(\Gamma_k\frac{\partial k}{\partial x_j}\right)+\tilde{G}_k-\rho\beta^* k\omega+S_k \tag{8}$$

$$\frac{\partial}{\partial t}(\rho\omega)+\frac{\partial}{\partial x_i}(\rho\omega u_i)=\frac{\partial}{\partial x_j}\left(\Gamma_\omega\frac{\partial\omega}{\partial x_j}\right)+\frac{\alpha}{\mu_t}G_k-\rho\beta\omega^2 + S_\omega+2(1-F_1)\rho\sigma_{\omega,2}\frac{1}{\omega}\frac{\partial k}{\partial x_j}\frac{\partial\omega}{\partial x_j} \tag{9}$$

where

$$\Gamma_k=\mu+\frac{\mu_t}{\sigma_k},\quad \Gamma_\omega=\mu+\frac{\mu_t}{\sigma_\omega},\quad \mu_t=\frac{\rho a_1 k}{\max\left[\frac{\omega a_1}{\alpha^*},SF_2\right]}, \tag{10}$$

$$\tilde{G}_k=\min\left(G_k,\epsilon c_1\right)\quad\text{and}\quad G_k=-\rho\overline{u_i{}'u_j{}'}\frac{\partial u_j}{\partial x_i}. \tag{11}$$

The only difference in the formulation of [20] with respect to [15] is the definition of the eddy viscosity μ_t. The version presented in [15] is shown in eq. (10), while in [20] vorticity is used instead of the strain rate S. The Prandtl numbers σ_k and σ_ω are obtained from

$$\sigma_k=\frac{1}{F_1/\sigma_{k,1}+(1-F_1)/\sigma_{k,2}}\quad\text{and}\quad \sigma_\omega=\frac{1}{F_1/\sigma_{\omega,1}+(1-F_1)/\sigma_{\omega,2}}, \tag{12}$$

while the blending functions F_1 and F_2 are given by

$$F_1=\tanh\left(\Phi_1^4\right);\quad \Phi_1=\min\left[\max\left(\frac{\sqrt{k}}{0.09\omega y},\frac{500\mu}{\rho y^2\omega}\right),\frac{4\rho k}{\sigma_{\omega,2}D_\omega^+ y^2}\right]; \tag{13}$$

$$F_2=\tanh\left(\Phi_2^2\right);\quad \Phi_2=\max\left[2\frac{\sqrt{k}}{0.09\omega y},\frac{500\mu}{\rho y^2\omega}\right]; \qquad D_\omega^+=\max\left[2\rho\frac{1}{\sigma_{\omega,2}}\frac{1}{\omega}\frac{\partial k}{\partial x_j}\frac{\partial\omega}{\partial x_j},10^{-10}\right] \tag{14}$$

and the model closure constants, which are set to assure agreement with known turbulence properties [11], are

$$\begin{aligned}&\sigma_{k,1}=1.176,\quad \sigma_{\omega,1}=0.5,\quad \sigma_{k,2}=1.0,\quad \sigma_{\omega,2}=0.8562,\quad \kappa=0.41,\\ &c_1=10,\gamma_1=0.5532,\quad \gamma_2=0.4403,\quad a_1=0.31,\\ &\beta_{i,1}=0.075\quad\text{and}\quad \beta_{i,2}=0.0828.\end{aligned} \tag{15}$$

2.3.2 Low-Reynolds-number correction

The low-Reynolds-number correction is carried out by the coefficient α^*, which damps the turbulent viscosity μ_t, and the coefficients α and β^*. The coefficient α^* controls the modeling of the effective diffusivity that determines the transport equations of the $k-\omega$ model, as explained in [11]. In the $k-\omega$ SST model, the turbulent viscosity μ_t is obtained as shown in eq. (10), and the coefficient α^* carries out the low-Reynolds-number correction on μ_t, which is obtained as

$$\alpha^* = \alpha^*_\infty \left(\frac{\alpha^*_0 + Re_T/R_k}{1 + Re_T/R_k} \right), \tag{16}$$

while the coefficient α determines the production of ω, as shown in eq. (9), and is given by

$$\alpha = \frac{\alpha_\infty}{\alpha^*} \left(\frac{\alpha_0 + Re_T/R_\omega}{1 + Re_T/R_\omega} \right), \tag{17}$$

and the coefficient β^* controls the dissipation of k (eq. (8)) and can be written as

$$\beta^* = \beta^*_\infty \left(\frac{100\beta_0/27 + (Re_T/R_\beta)^4}{1 + (Re_T/R_\beta)^4} \right), \tag{18}$$

where

$$Re_T = \frac{\rho k}{\mu\omega}, \quad R_k = 6, \quad \alpha^*_0 = \frac{\beta_i}{3}, \quad \beta_i = 0.072, \quad \alpha^*_\infty = 1, \quad \alpha_\infty = 0.52,$$
$$\alpha_0 = \frac{1}{9}, \quad R_\omega = 2.95, \quad \beta^*_\infty = 0.09, \quad \beta_0 = 0.0708, \quad \text{and} \quad R_\beta = 8. \tag{19}$$

being Re_T the turbulence Reynolds number. It must be noted that in high-Reynolds numbers, the value of the coefficient α^* is 1.

2.3.3 Curvature correction

This correction aims to deal with the insensitivity of the two-equation models to streamline curvature and system rotation, which are significant in turbulent flows. This is carried out by modifying the production term, as developed in [21], which is based on the works of [22] and [23].

In [22], an empirical function defined as "rotation function" was suggested to account for streamline curvature and system rotation effect, with the form

$$f_{\text{rotation}}(r^*, \hat{r}) = (1 + c_{r1}) \frac{2r^*}{1 - r^*} \left[1 - c_{r3} \tan^{-1}(c_{r2}\hat{r}) \right] - c_{r1}. \tag{20}$$

where the components $\hat{r}$ and r^* can be obtained as

$$\hat{r} = 2\Omega_{ik} S_{jk} \left[\frac{DS_{ij}}{Dt} + (\epsilon_{imn} S_{jn} + \epsilon_{jmn} S_{in}) \Omega^{Rot}_m \right] \frac{1}{\hat{D}} \quad \text{and} \quad r^* = \frac{S}{\Omega}, \tag{21}$$

where the vorticity tensor Ω and the strain-rate S are given by

$$\Omega^2 = 2\Omega_{ij}\Omega_{ij}, \quad \Omega_{ij} = \frac{1}{2}\left(\frac{\partial u_i}{\partial x_j} - \frac{\partial u_j}{\partial x_i}\right) + 2\epsilon_{mji}\Omega_m^{Rot}, \quad S^2 = 2S_{ij}S_{ij}, \tag{22}$$

and eq. (5). The constants for the $k-\omega$ SST model are $c_{r1} = 1$, $c_{r2} = 2$ and $c_{r3} = 1$, as established in [21]. This rotation function f_{rotation} is used to multiply the production term G_k (eq. (11)), given place to

$$G_k \rightarrow G_k \cdot f_{\text{rotation}}. \tag{23}$$

The implementation in ANSYS Fluent [19] limits the rotation function range from 0 to 1.25. These values represent, for instance, a strong convex curvature without turbulence production and a strong concave curvature with height turbulence production, respectively.

2.4 Transition SST model

The transition SST model was developed by [24] aiming to model the transition from laminar to turbulent flow in the shear layer. It is based on the coupling of the SST $k-\omega$ transport equations and two additional transport equations, one for the intermittency and other for the transition onset criteria. The transport equation for the intermittency γ is given by

$$\frac{\partial(\rho\gamma)}{\partial t} + \frac{\partial(\rho U_j\gamma)}{x_j} = P_{\gamma 1} - E_{\gamma 1} + P_{\gamma 2} - E_{\gamma 2} + \frac{\partial}{\partial x_j}\left[\left(\mu + \frac{\mu_t}{\sigma_\gamma}\right)\frac{\partial\gamma}{\partial x_j}\right] \tag{24}$$

where the transition and destruction or relaminarization sources are given by

$$\begin{aligned} &P_{\gamma 1} = C_{a1}F_{\text{length}}\rho S[\gamma F_{\text{onset}}]^{c_{\gamma 3}}, \qquad P_{\gamma 2} = C_{a2}\rho\Omega\gamma F_{\text{turb}} \\ &E_{\gamma 1} = C_{e1}P_{\gamma 1}\gamma, \qquad \text{and} \qquad E_{\gamma 2} = C_{e2}P_{\gamma 2}\gamma, \end{aligned} \tag{25}$$

where F_{length} is an empirical correlation that controls the length of the transition region and the constants are $C_{a1} = 2$ and $C_{e1} = 1$. Besides, the transition onset is controlled by the following relations:

$$F_{\text{turb}} = e^{-\left(\frac{R_T}{4}\right)^4}, \quad Re_v = \frac{\rho y^2 S}{\mu}, \quad Re_T = \frac{\rho k}{\mu\omega}, \quad F_{\text{onset1}} = \frac{Re_v}{2.193Re_{\theta_c}} \tag{26}$$

$$F_{\text{onset}} = \max\Bigg(\min\left(\max\left(F_{\text{onset1}}, F_{\text{onset1}}^4, 0\right), 2.0\right) - \max\left(1 - \left(\frac{R_T}{2.5}\right)^3, 0\right), 0\Bigg) \tag{27}$$

where Re_{θ_c} is the critical Reynolds number where the intermittency first starts to increase in the boundary layer and y is the wall distance. A summary of the

constants for these equations are:

$$C_{a1} = 2,\ C_{e1} = 1,\ C_{a2} = 0.06,\ C_{e2} = 50,\ C_{\gamma 3} = 0.5 \text{ and } \sigma_{\gamma} = 1.0. \quad (28)$$

The transport equations for the transition momentum thickness Reynolds number $R\tilde{e}_{\theta_c}$ is given by

$$\frac{\partial\left(\rho R\tilde{e}_{\theta_t}\right)}{\partial t} + \frac{\partial\left(\rho U_j R\tilde{e}_{\theta_t}\right)}{x_j} = P_{\theta 1} + \frac{\partial}{\partial x_j}\left[\sigma_{\theta t}\left(\mu + \mu_t\right)\frac{\partial R\tilde{e}_{\theta_t}}{\partial x_j}\right] \quad (29)$$

where the source terms are given by:

$$P_{\theta 1} = c_{\theta 1}\frac{\rho}{t}\left(Re_{\theta_t} - R\tilde{e}_{\theta_t}\right)\left(1.0 - F_{\theta 1}\right), \quad t = \frac{500\mu}{\rho U^2}, \quad F_{\text{wake}} = e^{-\left(\frac{Re_{\omega}}{10^5}\right)^2} \quad (30)$$

$$F_{\theta 1} = \min\left(\max\left(F_{\text{wake}}e^{\left(-\frac{y}{\delta}\right)^4}, 1.0 - \left(\frac{\gamma - 1/50}{1.0 - 1/50}\right)^2\right), 1.0\right) \quad (31)$$

$$\theta_{BL} = \frac{R\tilde{e}_{\theta_t}\mu}{\rho U}, \quad \delta_{BL} = \frac{15}{2}\theta_{BL}, \quad \delta = \frac{50\Omega_y}{U}\delta_{BL}, \quad \text{and} \quad Re_{\omega} = \frac{\rho\omega y^2}{\mu}. \quad (32)$$

where the constants of this equation are $C_{\theta t} = 0.03$ and $\sigma_{\theta t} = 2.0$. The boundary conditions for $R\tilde{e}_{\theta_t}$ at a wall is zero flux. The model contains three empirical correlations provided and detailed in [25].

3 Numerical modeling

A conceptual scheme of the flow domain and boundary conditions employed in this study is shown in figure 4. The dimensions of the flow domain are $30B$ by $40B$, being B the width of the cross-section. The inlet is placed at the left side of the flow domain, considering a Dirichlet condition with a constant velocity of 4.4 m/s, a turbulence intensity of 1% and a turbulence length scale of $0.1B$. A pressure outlet is located at the right side of the computational domain with imposed atmospheric pressure. The upper and lower limits of the domain represent slip walls. The corners of the semicircular cross-section have been modeled as sharp corners. The wall boundary condition on the section edge has been modeled by integration to the surface by means of a low turbulent Reynolds number formulation [26].

4 Geometry, mesh description and verification studies

Six different sections with circular segment shape and sharp corners, as described in figure 1, are analyzed in this work. Thus, six meshes have been generated, and three of them verificated in order to assess the independence of the results with the spatial discretization, which correspond to $\beta = [40°, 60°, 90°]$. A structured mesh has been adopted for the region attached to the bluff body and the outer part of the

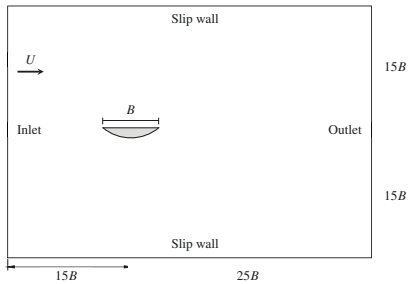

Figure 4: Definition of the flow domain and boundary conditions (not to scale).

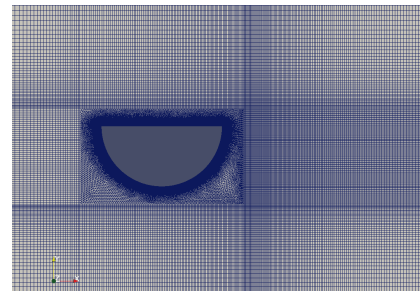

Figure 5: Mesh of $\beta = 90°$ section. Detail of the buffer and exterior area.

Table 1: Properties and results of the grid-refinement study for the D-section ($\beta = 90°$).

Grid	Total cells	BL cells	St	f [Hz]	C_L	C_D	C_M	C_L'	C_D'	C_M'
Coarse	199 689	70 200	0.217	5.615	0.676	0.440	0.153	0.314	0.041	0.049
Medium	270 098	86 000	0.211	5.466	0.672	0.437	0.153	0.314	0.041	0.049
Fine	362 789	104 800	0.210	5.451	0.677	0.442	0.155	0.321	0.041	0.050
Experimental			0.212	5.491	0.670	0.450	0.116	-	-	-

flow domain. On the other hand, an unstructured triangular mesh has been adopted for the buffer zone that lays in between the two regions previously mentioned.

The result of the verification study carried out for the $\beta = 90°$ section is shown in table 1, where the number of total cells employed on each mesh is shown along with the cells around the deck and the values obtained of the aerodynamic coefficients and its standard deviation, indicated with the prime symbol. The main discrepancies shown in the verifications of the three sections take place between the coarse and medium meshes, presenting good agreement the results of the medium with regards to the finest mesh in all cases. Therefore, the medium meshed can be employed for further analyses while the coarse mesh has been disregarded. In the verification study Menter's SST $k - \omega$ model has been adopted. It must be noticed that the number of elements used for the coarse mesh is above the usual values adopted in equivalent verification studies.

Hence, the meshes employed in this work have an average number of cells of $3 \cdot 10^5$ and a summary of their main properties is presented in table 2. The mesh corresponding to $\beta = 90°$ is shown in figure 5. The first layer of cells has a dimensionless height of $\delta_1/B = 3.235{\cdot}10^{-4}$, where δ_1 is the height of the first grid

WIT Transactions on Engineering Sciences, Vol 105, © 2016 WIT Press
www.witpress.com, ISSN 1743-3533 (on-line)

Table 2: Properties of the meshes for each section, where BL is the boundary layer mesh, P means perimeter, h_1 is the height of the first element, H is the height of the boundary layer mesh, No. is the number of elements vertically and r the growing ratio.

	Number of cells				Boundary layer definition					y^+		
$\beta[^\circ]$	Total	BL	Buffer	Exterior	P	h_1/B	H/B	No.	r	Mean	Max	$y^+ > 4[\%]$
40	321 050	113 680	72 370	135 000	1960	$3.24 \cdot 10^{-4}$	$3.82 \cdot 10^{-2}$	58	1.02	1.50	6.04	10.20
50	318 809	113 680	70 129	135 000	1960	$3.24 \cdot 10^{-4}$	$3.82 \cdot 10^{-2}$	58	1.02	1.45	6.22	10.20
60	296 846	99 760	62 086	135 000	1720	$3.24 \cdot 10^{-4}$	$3.82 \cdot 10^{-2}$	58	1.02	1.26	6.45	17.44
70	314 927	113 680	66 247	135 000	1960	$3.24 \cdot 10^{-4}$	$3.82 \cdot 10^{-2}$	58	1.02	1.24	6.47	20.41
80	272 288	86 000	51 288	135 000	1720	$3.24 \cdot 10^{-4}$	$3.82 \cdot 10^{-2}$	50	1.03	1.31	5.93	17.44
90	270 098	86 000	49 098	135 000	1720	$3.24 \cdot 10^{-4}$	$3.82 \cdot 10^{-2}$	50	1.03	1.35	6.38	29.07

layer, and dimensionless wall distances $y^+ = (\delta_1 u_*)/\nu$, where u_* is the friction velocity, present mean values lower than 1.5 and maximum values are lower than 6.5 for the considered Reynolds number $Re = 1 \cdot 10^5$. A maximum Courant number of $Co = 1$ was considered, which leads to a mean non-dimensional time step values in the range $\bar{\Delta}s = \bar{\Delta}tU/B = \left[1.7 \cdot 10^{-4}, 2.7 \cdot 10^{-4}\right]$, depending on the considered simulation.

5 Results and validation with wind tunnel data

The results of sections $\beta = [40°, 60°, 90°]$ are validated with wind tunnel tests carried out in the wind tunnel of the University of La Coruña, and reported in [27]. The models where built employing foamed PVC plates and aluminum bars, and they are 1 m long and 0.33 m wide. Special care has been taken during the construction with the sharp corners geometry and smooth surfaces. The curved geometry is achieved by bending thick foamed PVC plates over the internal curved foamed PVC ribs that define the geometry of the model.

The wind tunnel is an open circuit tunnel with a test chamber of 2x1x1 m^3 in open configuration, and the tests where carried out with a wind velocity of 4.4 m/s in smooth flow, which correspond to the Reynolds number employed in the CFD analyses of $Re = 1 \cdot 10^5$, achieved with a contraction rate of 6:1 in the nozzle after the flow conditioners.

As described in [28], the aerodynamic coefficients of circular geometries are very sensitive to Reynolds number effects. In order to know the influence of this parameter on the results, an study of the Reynolds number effects of the three tested models have been carried out. Given that the sections are circular segments, and the changes in the regime are controlled by changes in the location of the flow separation in the circular side of the geometry, the Reynolds number effects should occur at similar Reynolds numbers in the three sections. Formulating the Reynolds number with respect to the radius of the circular segment Re_R, in order to use a curvature-related dimension, it was found that the regime change happens at approximately the same Reynolds number, about $Re_R = 2 \cdot 10^5$, which correspond to Reynolds numbers with respect to the section width in the range of $Re = \left[2.5 \cdot 10^5, 4 \cdot 10^5\right]$ for the three sections. Given that the tests were carried out at a flow velocity of 4.4 m/s, which correspond to $Re = 1 \cdot 10^5$ with respect to the width of the three sections, it can be concluded that the test where done in the sub-critical regime.

The results obtained in the wind tunnel, and those from the CFD, are also checked with some results reported in the literature, such as [2–6, 29]. A summary of the results obtained with $k - \omega$ SST model, and including some corrections in the turbulence model along with the wind tunnel test, are reported in table 3.

Table 3: Summary of aerodynamic coefficients obtained numerically and experimentally.

Section	Attack	C_L			C_D			C_M			St		
		Exp	SST	Corr.	Exp	SST	Corr.	Exp	SST	Corr.	Exp	SST	Corr.
	$\alpha = 0°$	0.672	0.672	-	0.456	0.437	-	0.117	0.152	-	0.210	0.211	-
$\beta = 90°$	$\alpha = 1°$	0.613	0.648	-	0.481	0.450	-	0.098	0.129	-	0.205	0.206	-
	$\partial/\partial\alpha\|_{\alpha=0°}^{\Delta\alpha=1°}$	−3.383	−1.400	-	1.470	0.736	-	−1.077	−1.323	-			
	$\alpha = 0°$	-	0.406	-	-	0.294	-	-	0.145	-	-	0.206	-
$\beta = 80°$	$\alpha = 1°$	-	0.489	-	-	0.353	-	-	0.160	-	-	0.201	-
	$\partial/\partial\alpha\|_{\alpha=0°}^{\Delta\alpha=1°}$	-	4.722	-	-	3.379	-	-	0.859	-			
	$\alpha = 0°$	-	0.368	-	-	0.201	-	-	0.130	-	-	0.180	-
$\beta = 70°$	$\alpha = 1°$	-	0.363	-	-	0.222	-	-	0.124	-	-	0.182	-
	$\partial/\partial\alpha\|_{\alpha=0°}^{\Delta\alpha=1°}$	-	−0.292	-	-	1.152	-	-	−0.300	-			
	$\alpha = 0°$	0.277	0.287	0.280 [L]	0.219	0.137	0.247 [L]	0.123	0.126	0.169 [L]	0.197	0.022	0.210 [L]
$\beta = 60°$	$\alpha = 1°$	0.407	0.319	0.517 [C]	0.221	0.150	0.274 [C]	0.128	0.117	0.157 [C]	0.191	0.024	0.201 [C]
	$\partial/\partial\alpha\|_{\alpha=0°}^{\Delta\alpha=1°}$	7.423	1.816	13.556	0.141	0.716	1.522	0.250	−0.539	−0.705			
	$\alpha = 0°$	-	−0.241	0.068 [T]	-	0.099	0.127 [T]	-	0.102	0.135 [T]	-	0.446	0.223 [T]
$\beta = 50°$	$\alpha = 1°$	-	0.025	0.305 [T]	-	0.098	0.129 [T]	-	0.123	0.146 [T]	-	0.015	0.000 [T]
	$\partial/\partial\alpha\|_{\alpha=0°}^{\Delta\alpha=1°}$	-	15.223	13.573	-	−0.071	0.128	-	1.164	0.642			
	$\alpha = 0°$	0.039	−0.322	−0.049 [L]	0.103	0.056	0.105 [L]	0.086	0.064	0.116 [L]	0.223	0.310	0.243 [L]
$\beta = 40°$	$\alpha = 1°$	0.107	-	0.048 [C]	0.106	-	0.112 [C]	0.102	-	0.134 [C]	0.219	-	0.238 [C]
	$\partial/\partial\alpha\|_{\alpha=0°}^{\Delta\alpha=1°}$	3.926	-	5.549	0.171	-	0.404	0.889	-	1.031			

[L] The $k - \omega$ SST turbulence model has been implemented with low-Reynolds-number correction. [C] The $k - \omega$ SST turbulence model has been implemented with low-Reynolds-number and curvature correction. [T] Transition SST turbulence model.

WIT Transactions on Engineering Sciences, Vol 105, © 2016 WIT Press
www.witpress.com, ISSN 1743-3533 (on-line)

6 Impact of curvature and low Reynolds corrections

The performance of the turbulence model and the corrections applied to it can be noted when comparing the results obtained experimentally with those obtained numerically employed the $k-\omega$ SST turbulent model, which are shown for $\alpha = 0°$ and $\alpha = 1°$ in table 3.

Focusing firstly in the $\beta = 90°$ section for $\alpha = 0°$, the $k - \omega$ SST turbulence model offers a good agreement for the Strouhal number and lift and drag coefficients. The moment coefficient presents an absolute error of $\Delta_{\mathrm{Cm}} = 0.035$, which can be assumed as acceptable, taking into account the inherent limitation in the 2D approach, the two-equation turbulence modeling and the uncertainty in the effective degree of sharpness in the wind tunnel models or the effective angle of attack. Besides, the results obtained for $\alpha = 1°$ with the $k - \omega$ SST turbulence model are also acceptable.

In the case of the $\beta = 40°$ section for $\alpha = 0°$, it can be seen in table 3 that the $k - \omega$ SST model do not provide an acceptable value for the Cl and the Strouhal number is far from the experimental one. Besides, Cd and Cm values are neither accurate enough. However, when applying the low-Reynolds-number correction over the model, notable improvements are obtained, and the results can be successfully compared with the wind tunnel data. However, when considering an incident angle of $\alpha = 1°$, the curvature correction is also required to achieve a good agreement with the experimental value.

The case of $\beta = 60°$ presents and intermediate situation where the results of the $k-\omega$ SST model with and without corrections are very similar between them, and to the experimental results. A good result is obtained for $\alpha = 0°$ in the value of Cl with or without corrections, as shown in table 3. The result of the Cd obtained with $k-\omega$ SST model with low-Reynolds-number correction is more accurate, but, on the other hand, the $k - \omega$ SST model performs better without any correction for obtaining the Cm. For $\alpha = 1°$, both results are also acceptable, although the Strouhal number is only acceptable when applying the low-Reynolds-number and curvature corrections, as it happens also for $\alpha = 0°$.

Based on these results, the values of β between $90°$ and $70°$ are obtained with the $k - \omega$ SST turbulence model without applying corrections. In the $\beta = 50°$ case, it has been found that applying the four-equation transition SST model better results are achieved than with the $k - \omega$ SST with or without corrections. Thus, the results presented in table 3 in the Corrections column for the $\beta = 50°$ case are obtained with this four-equation model.

7 Conclusions

In this work, the force coefficients and Strouhal numbers of several circular segments, which correspond to a simplified bridge deck cross section, whose shape is defined by a geometry parameter β, have been computed based on a 2D URANS approach, employing Menter's $k - \omega$ SST turbulence model. Several

meshes combining structured regions with a non-structured buffer zone have been used and the CFD solvers employed were Fluent and Open FOAM.

The results have been validated with wind tunnel test results in order to ascertain their accuracy. Besides, low-Reynolds-number correction and curvature correction have been applied to the $k-\omega$ SST turbulence model in order to improve the results and assess their influence. It has been seen that depending on the analyzed section, the influence of the corrections over the model varies. In particular, the results of $\beta = 90°$ section are insensitive to the corrections in the turbulence model, while the results of $\beta = 40°$ section are very dependent on these corrections. In the middle point, the $\beta = 60°$ section present slight variations when the correction are used.

Therefore, in order to characterize the aerodynamic coefficients in the range of the design domain, which is $\beta = [40°, 90°]$, the aerodynamic coefficients for the sections in the range $\beta = [40°, 60°]$ at $\alpha = 0°$ are obtained using the $k - \omega$ SST turbulence model employing the low-Reynolds-number corrections, while the in range $\beta = [70°, 90°]$ the corrections are not required. Besides, when assessing these models for a wind incident angle of $\alpha = 1°$, sections of $\beta = 60°$ and $\beta = 40°$ also need the curvature corrections. Furthermore, in the particular case of $\beta = 50°$, the four-equation transition SST model achieve better results than the $k - \omega$ SST model with or without corrections.

Acknowledgements

The research leading to these results has received funding from the Spanish Minister of Economy and Competitiveness (MINECO) with reference BIA2013-41965-P, the Fundación Pedro Barrié de la Maza and the Universidade da Coruña. The authors fully acknowledge the support received.

References

[1] Hernández, S., Cid, M., Nieto, F. & Jurado, J.A., Optimization of stays and deck shape in cable supported bridges including structural and aeroelastic constraints. *BBAA8, 8^{th} International Colloquium on Bluff Body Aerodynamics and Applications*, 2016.

[2] Den Hartog, J.P., Transmission line vibration due to sleet. *AIEE Transactions*, **(51)**, pp. 1074–1086, 1932.

[3] Richardson, A.S. & Martuccelli, J.R., Research study on galloping of electric power transmission lines. *Conference on wind effects on buildings and structures*, 1963.

[4] Novak, M. & Tanaka, H., Effect of turbulence on galloping instability. *Journal of the engineering mechanics division*, **100(1)**, pp. 27–47, 1974.

[5] Weaver, D. & Veljkovic, I., Vortex shedding and galloping of open semi-circular and parabolic cylinders in cross-flow. *Journal of fluids and structures*, **21**, pp. 65–74, 2005.

[6] Ali, M., Arafa, M. & Elaraby, M., Harvesting energy from galloping oscillations. *Proceedings of the world congress on engineering, WCE 2013, London, UK*, 2013.
[7] Pantaleón, M.J., Revilla, R. & Olazábal, P., Santander Bay's Footbridge. *Structural Engineering International*, **24(1)**, pp. 96–97, 2014.
[8] Anderson, J.D., *Computational fluid dynamics. The basics and applications.* McGraw-Hill, Inc., 1995.
[9] Wilcox, D.C., *Elements of Fluids Mechanics*. DCW Industries Inc., La Cañada, CA, USA, 2005.
[10] Versteeg, H.K. & Malalasekera, W., *An introduction to Computational Fluid Dynamics: The finite volume method. 2^{th} edition.* Pearson Education Limited, UK, 2007.
[11] Wilcox, D.C., *Turbulence Modeling for CFD, third edition.* DCW Industries Inc., 2006.
[12] Spalart, P.R. & Allmaras, S.R., One-equation turbulence model for aerodynamic flows. *Recherche Aerospatiale*, **1**, pp. 5–21, 1994.
[13] Yakhot, V. & Orszag, S.A., Renormalization group analysis of turbulence: basic theory. *Journal of Scientific Computing*, **1**, pp. 3–11, 1986.
[14] Wilcox, D.C., Reassessment of the scale-determining equation for advanced turbulence models. *AIAA Journal*, **26(11)**, pp. 1299–1310, 1988.
[15] Menter, F.R., Two-equation eddy-viscosity turbulence models for engineering applications. *AIAA Journal*, **32(8)**, pp. 1598–1605, 1994.
[16] Menter, F.R., Kuntz, M. & Langtry, R., Ten years of industrial experience with the SST turbulence model. *Turbulence, heat and mass transfer, vol. 4. Redding (CT, USA), Begell House Inc.*, pp. 625–632, 2003.
[17] Xu, Y.L., *Wind effects on cable-supported bridges*. John Wiley & Sons, Singapore, 2013.
[18] OpenFOAM Foundation Ltd., *OpenFOAM User Guide*, 2015.
[19] ANSIS, Inc., Canonsburg, PA, USA, *ANSYS Fluent Theory Guide*, 2013.
[20] Menter, F. & Esch, T., Elements of industrial heat transfer prediction. *Sixteenth Brazilian congress of mechanical engineering*, 2001.
[21] Smirnov, P.E. & Menter, F.R., Sensitization of the SST turbulence model to rotation and curvature by applying the Spolart-Shur correction term. *ASME Paper GT 1008-50480. Berlin, Germany*, 2008.
[22] Spalart, P.R. & Shur, M., On the sensitization of turbulence models to rotation and curvature. *Aerospace Science and Technology*, **5**, pp. 297–302, 1997.
[23] Shur, M.L., Strelets, M.K. & Travin, A.K., Turbulence modeling in rotational and curved channels: Assessing the Spalart-Shur correction. *AIAA Journal*, **38**, pp. 784–792, 2000.
[24] Menter, F.R., Langtry, R.B., Likki, S.R., Suzen, Y.B., Huang, P.G. & Völker, S., A correlation-based transition model using local variables- part I: Model formulation. *Journal of Turbomachinery (ASME)*, **(128)**, pp. 413–422, 2006.

[25] Langtry, R.B. & Menter, F.R., Correlation-based transition modeling for unstructured parallelized fluid dynamic codes. *AIAA Journal*, **(47)**, pp. 2894–2906, 2009.
[26] Jones, W.P. & Launder, B.E., The prediction of laminarization with a two-equations model of turbulence. *International Journal of Heat and Mass Transfer*, **(15)**, pp. 301–314, 1972.
[27] Jurado, J.A., Sánchez, R., Cid, M., Hernández, S. & Nieto, F., Wind tunnel test of bridge deck sectional models with semicircular profile. *ICWE14, 14th International Conference on Wind Engineering*, 2014.
[28] Zdravkovich, M.M., *Flow around circular cylinders. Vol 1: Fundamentals*. Oxford Science Publications, 1997.
[29] Ratkowski, J.J., Experiments with galloping spans. *IEEE Transactions on Power Apparatus and Systems*, 1963.